

Title	Modeling characterisation of a bipolar pulsed discharge
Author(s)	Donkó, Zoltán; Zajičková, Lenka; Sugimoto, Satoshi et al.
Citation	Plasma Sources Science and Technology. 29(10) p.104001
Issue Date	2020-10-16
oaire:version	VoR
URL	<a href="https://hdl.handle.net/11094/78268">https://hdl.handle.net/11094/78268</a>
rights	© 2020 The Author(s). Original content from this work may be used under the terms of the Creative Commons Attribution 4.0 licence. Any further distribution of this work must maintain attribution to the author(s) and the title of the work, journal citation and DOI.
Note	

***Osaka University Knowledge Archive : OUKA***

<https://ir.library.osaka-u.ac.jp/>

Osaka University

PAPER • OPEN ACCESS

## Modeling characterisation of a bipolar pulsed discharge

To cite this article: Zoltán Donkó *et al* 2020 *Plasma Sources Sci. Technol.* **29** 104001

View the [article online](#) for updates and enhancements.



**IOP | ebooks™**

Bringing together innovative digital publishing with leading authors from the global scientific community.

Start exploring the collection—download the first chapter of every title for free.

# Modeling characterisation of a bipolar pulsed discharge

Zoltán Donkó<sup>1,2,\*</sup> , Lenka Zajíčková<sup>3</sup> , Satoshi Sugimoto<sup>2</sup>,  
Anjar Anggraini Harumningtyas<sup>2,4</sup>  and Satoshi Hamaguchi<sup>2</sup> 

<sup>1</sup> Institute for Solid State Physics and Optics, Wigner Research Center for Physics, 1121 Budapest, Konkoly-Thege Miklós street 29-33, Hungary

<sup>2</sup> Center for Atomic and Molecular Technologies, Graduate School of Engineering, Osaka University, 2-1 Yamadaoka, Suita, Osaka 565-0871, Japan

<sup>3</sup> Faculty of Science & CEITEC, Masaryk University, Brno, Czech Republic

<sup>4</sup> Center for Accelerator Science and Technology, National Nuclear Energy Agency of Indonesia (BATAN) Babarsari Kotak Pos 6101 ykbb Yogyakarta 5528181, Indonesia.

E-mail: [donko.zoltan@wigner.hu](mailto:donko.zoltan@wigner.hu)

Received 4 June 2020, revised 7 August 2020

Accepted for publication 27 August 2020

Published 16 October 2020



## Abstract

We apply particle based kinetic simulations to explore the characteristics of a low-pressure gas discharge driven by high-voltage ( $\sim$ kV) pulses with alternating polarity, with a duty cycle of  $\approx$  1% and a repetition rate of 5 kHz. The computations allow tracing the spatio-temporal development of several discharge characteristics, the potential and electric field distributions, charged particle densities and fluxes, the mean ion energy at the electrode surfaces, etc. As such discharges have important surface processing applications, e.g. in the treatment of artificial bones, we analyse the time-dependence of the flux and the mean energy of the ions reaching the electrode surfaces, which can be both conducting and dielectric. Our investigations are conducted for argon buffer gas in the 40–140 Pa pressure range, for 1–5 cm electrode gaps and voltage pulse amplitudes ranging between 600 V and 1200 V.

Keywords: pulsed waveform, kinetic simulation, numerical modeling

(Some figures may appear in colour only in the online journal)


## 1. Introduction

Low-pressure gas discharges have widely been used for surface processing/modification [1–17]. These plasma sources may operate with various types of excitation. The simplest case is represented by the direct-current (DC) excitation, which can create plasmas between conducting electrodes. Alternating-current (AC) excitation offers the possibility to create plasmas between dielectric surfaces as well. High-frequency plasma sources (e.g. capacitively and inductively coupled), which typically operate within the 1–100 MHz ‘radio-frequency’ (RF) domain, are most widespread in, e.g. microelectronics,

solar cell production, surface modification of medical implants and other areas in which plasma etching or plasma enhanced chemical vapor deposition proved to be useful [16]. The importance of ion energy was clearly demonstrated in several applications including plasma etching [2, 7, 9, 12, 18–21] and plasma assisted deposition [4, 5, 8, 11, 22, 23]. Although the bombardment of energetic ions is usually avoided in plasma polymerization and the role of ions is disregarded, some authors emphasize the role of ions in the mass deposition rate [23] or cross-linking caused by the energy flux per deposited atom [24]. Recent advancements in plasma polymerization emphasized the importance of ions for creation of radical-functionalized plasma polymers [25].

In RF plasmas, voltage waveform tailoring [26–30], i.e., the synthesis of complex waveforms from a harmonic signal of a given base frequency and its harmonics with given amplitudes and phases has proven to be an efficient approach for

\* Author to whom any correspondence should be addressed.

 Original content from this work may be used under the terms of the [Creative Commons Attribution 4.0 licence](https://creativecommons.org/licenses/by/4.0/). Any further distribution of this work must maintain attribution to the author(s) and the title of the work, journal citation and DOI.

controlling the charged particle dynamics, power absorption, the generation of active species, as well as for optimising the charged particle fluxes and energy distribution functions at plasma facing surfaces both at low [31–35] and high [36, 37] pressures.

The time-dependence of the excitation provides an extra degree of freedom for the control of the charged particle dynamics. Both the DC and AC excitation can be continuous, modulated, or pulsed. Designing a specific waveform for the excitation may have a number of advantages. In the field of magnetron sputtering, e.g., it was realised that pulsed excitation, ‘high power impulse magnetron sputtering’, allows creating significantly higher particle densities and fluxes as compared to DC sputtering [38, 39]. In the field of gas lasers, pulsed excitation is common for cases of self-terminating transitions [40]. In capillary vacuum-ultraviolet lasers very short high-voltage pulses provide conditions for population inversion [41, 42]. Discharges with dielectric electrode surfaces (‘dielectric barrier discharges’) exhibit self-terminating characteristics due to the charging of the insulating surfaces. Thus, despite their excitation is continuous (a simple sine wave voltage waveform) the current through the discharge flows during limited time [43–45]. Discharges generated by various short-pulse waveforms [46–57] have found applications in combustion [58, 59], aerodynamic flow control [60, 61], switching [62, 63], spectroscopy [64–67], synthesis of nanomaterials [68], conversion of gases [69, 70] as well as in biomedical applications through the generation of reactive species at ambient pressure and temperature [71–76].

A very important line of research has been focusing on the surface treatment of medical implants, where mechanical properties and biocompatibility of certain materials can significantly be improved [77, 78]. Plasma immersion ion implantation of metallic osteosynthesis plates has been reported in [79]. Plasma treatment has been applied as well for special alloys that are of interest in spinal deformity correction and for cardiovascular materials (used, e.g., for artificial heart valves) [80] and in tissue engineering [81]. Plasma spraying [82], dielectric barrier discharges [83, 84] and low-pressure pulsed discharges [85, 86] have been applied for the treatment of artificial bones.

In some applications, processing at low surface temperature is a crucial requirement. For example, polystyrene has a melting point at approximately 240 °C. Therefore plasma surface treatment of polystyrene must be performed at temperature much lower than 240 °C to avoid any deformation of the treated material or degradation of its surface chemical composition. Typically power consumption by the plasma is a good indicator of the processing temperature. Pulsed discharges with sufficiently low duty cycles may be used for such low-temperature processes, especially if the afterglow plasma (i.e., plasma that remains during the absence of the applied electric field) contributes to the surface process such as material deposition or surface polymerization.

Recent study on the surface modification of artificial bone made of porous hydroxyapatite (HA) was performed using parallel-plate pulsed discharges with a mixed gas containing methane, nitrogen, and helium, where amine containing

polymers were deposited on the surface of artificial bone [85, 86]. The typical discharge conditions were the following; gap of the conducting parallel plate electrodes 38 mm; magnitude of applied bipolar voltage approximately 1 kV (such that the peak-to-peak voltage 2 kV); single pulse duration 1  $\mu$ s; duty cycle 1%; gas pressure 70 Pa. The observed polymer deposition rate on the outer surface of artificial bone was approximately 3 nm min<sup>−1</sup>. The discharges under these conditions also permitted the reactive plasma gas to penetrate into the inner pores of HA and polymerization occurred on the surfaces of inner pores whose diameters were in the range from 40 to 150  $\mu$ m.

These observations have motivated our study that aims to uncover the connection between external control parameters (gas pressure, voltage pulse amplitude, electrode gap) and ion properties (flux, mean energy, and energy distribution) at the surfaces. To minimise the number of plasma-chemical processes, we conducted the simulations for a simple discharge gas (argon) as used in the earlier plasma-processing experiments [87, 88]. However, the results should present a detailed insight into the essential nature of pulsed plasma discharges in general, including those used for plasma polymerization on artificial bone [85, 86].

In this work, we present a numerical study of discharges established by  $\sim 1 \mu$ s high voltage (600 V–1200 V) pulses in argon gas at pressures between 40 Pa and 140 Pa. The plasma is created between two parallel plate electrodes (see figure 1). The powered electrode is conducting, while the surface of the grounded electrode can be both, conducting or dielectric. The excitation voltage pulses follow each other with alternating polarity and 100  $\mu$ s delay between the pulses. The voltage pulse shape is adopted from a measurement using the apparatus described in [89, 90].

The paper is structured as follows. The simulation method is described in section 2. The results are presented in section 3, in two parts. A detailed analysis of the physics of the discharge is presented for a base set of conditions, in section 3.1, while the effect of the excitation voltage pulse amplitude, the gas pressure, and the electrode gap length on selected discharge characteristics are discussed in section 3.2. Finally, a brief summary is given in section 4.

## 2. Simulation method

The discharge is described by the ‘standard’ 1d3v particle-in-cell simulation approach combined with the Monte Carlo treatment of collisions [91–93]. The working gas is argon, which is supposed to have uniform spatial density and a temperature of  $T_g = 350$  K. The ‘active’ species in the simulation are electrons and Ar<sup>+</sup> ions. The electron impact cross sections are adopted from [94]. This set includes the elastic momentum transfer cross section, one excitation cross section that is the sum of all excitation cross sections, and the ionisation cross section. The e<sup>−</sup> + Ar collisions are assumed to result in isotropic scattering. In the case of Ar<sup>+</sup> + Ar collisions only elastic collisions are considered. The cross section set includes an isotropic scattering part, as well as a backward scattering part [95].

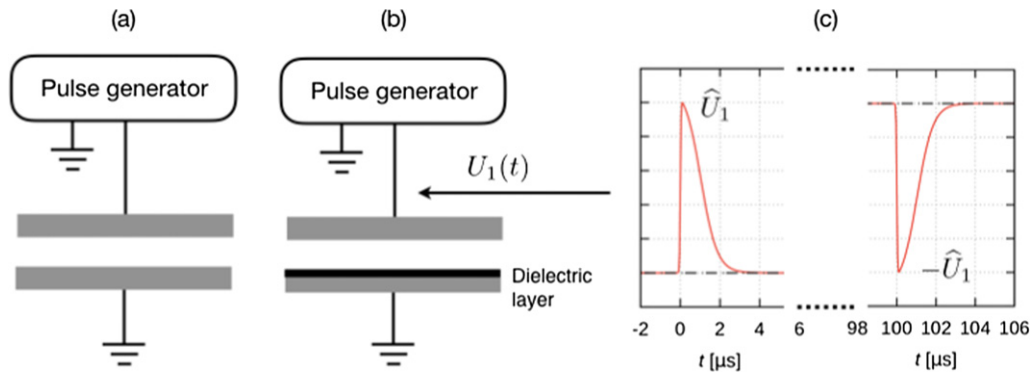


**Figure 1.** The discharge between the parallel plate electrodes is created by a repetitive voltage pulses having alternating polarity. The upper (powered) electrode is conducting, the lower (grounded) electrode is either conducting (a) or may have a thin dielectric layer over its surface (b). Panel (c) shows a pair of positive/negative excitation voltage pulses, which have  $\hat{U}_1$  and  $-\hat{U}_1$  peak amplitudes, respectively, and are displaced by a delay of 100  $\mu\text{s}$ . Pairs of such pulses follow each other with  $f = 5$  kHz repetition rate (i.e. the ‘fundamental period’ is 200  $\mu\text{s}$ ).

The electrodes of the discharge are parallel plates, situated at a distance  $L$  from each other. As already mentioned in section 1, two configurations are considered: in the first case both electrodes are conducting, while in the second case one of the electrodes is supposed to be covered by a dielectric layer. This layer is modelled as a capacitor that has a value of  $C = 10$  pF for a unit area of  $A_0 = 1$  cm<sup>2</sup>. (This capacitance corresponds to a  $\approx 1$  mm-thick polystyrene layer that has a relative permittivity of 2.56.) The capacitor is treated in the simulations as an additional circuit element. Its initial charge is taken to be zero, and during the simulations the voltage drop over it is computed from the time integral of the currents (including both the conduction and displacement components) from the plasma to its surface. For both electrodes a constant ion-induced secondary electron emission coefficient ( $\gamma$ ) is defined. For a conducting surface  $\gamma$  is taken to be 0.07, while for a dielectric surface  $\gamma = 0.3$  is assumed. Electrons reaching the electrode surfaces are elastically reflected with a probability of  $\eta = 0.2$  [96].

The simulation uses a spatial grid with 1200 points and the length of the  $T = 200$   $\mu\text{s}$  fundamental period comprises  $2 \times 10^7$  time steps. The number of simulation particles is between  $10^5$  and  $3 \times 10^5$ . Convergence is typically reached during tens of periods. Due to the very low duty cycle ( $\sim 1\%$ ) the simulation (convergence + data collection phases) of a single case with the above settings takes several months on a single CPU. The main results of the simulations are spatiotemporal distributions of selected discharge characteristics (e.g. the electron density and the ionisation source function), as well as the flux and the energy distribution of the ions hitting the electrode surfaces. These characteristics are studied as a function of the operating conditions (nature of electrode surfaces, gas pressure, electrode gap, and voltage peak amplitude).

### 3. Results

In the following section 3.1, we illustrate the main discharge characteristics for the case of  $\hat{U}_1 = 1000$  V,  $p = 100$  Pa, and  $L = 3$  cm, which is considered here as the ‘base case’. Subsequently in section 3.2, we present a parameter variation, where

we study the effects of the gas pressure, the voltage pulse amplitude, as well as the electrode separation.

#### 3.1. Characterisation of the discharge behaviour

Here, for the ‘base case’ defined above, we compare the properties of the discharge with different electrodes. The powered electrode is taken to be conducting in all cases, and is characterised with a secondary electron emission coefficient of  $\gamma_p = 0.07$  [97, 98]. This value is typical for Ar<sup>+</sup> ion bombardment of metal surfaces at moderate energies up to hundreds of eV-s [97]. For the other electrode that is connected to ground potential, we consider both conducting and dielectric surfaces. In the former case, we assume  $\gamma_g = \gamma_p = 0.07$ , while in the latter we chose a higher secondary electron emission yield typical for dielectric materials,  $\gamma_g = 0.3$ . (The ‘p’ and ‘g’ subscripts refer to the powered and grounded electrodes, respectively.)

For an additional test case,  $\gamma_g = 0.07$  is used instead of  $\gamma_g = 0.3$  for the grounded electrode with a dielectric layer. This test is supposed to check the correctness of the simulation: at equal secondary yields at both electrodes the same gap voltage is expected irrespective of which surface is covered by the dielectric layer. Thus time-shifted but spatially symmetrical patterns are expected from the simulation.

Figure 2 shows the relevant voltage waveforms at the electrode surfaces and over the discharge gap. Panels in the left column (a), (c), (e) present the data for the vicinity of the positive excitation pulse, while panels in the right column (b), (d), (f) shows the same data in the vicinity of the negative excitation pulse. The voltage waveform applied to the powered electrode,  $U_1$ , has in this ‘base’ case  $\pm 1000$  V peak amplitude and a width of  $\approx 1$   $\mu\text{s}$ . The shape of the excitation waveform has been adopted from experiments [89], and is kept the same throughout our studies, only the peak amplitude is varied in section 3.2. The positive and negative pulses have exactly the same shape, only their polarity differs. The positive pulse is applied at  $t = 0$   $\mu\text{s}$ , whereas the negative pulse appears at  $t = 100$   $\mu\text{s}$ . The pulses repeat with the (fundamental) period of 200  $\mu\text{s}$ , corresponding to a repetition rate of  $f = 5$  kHz that is typically used in the current experiments [85, 86].



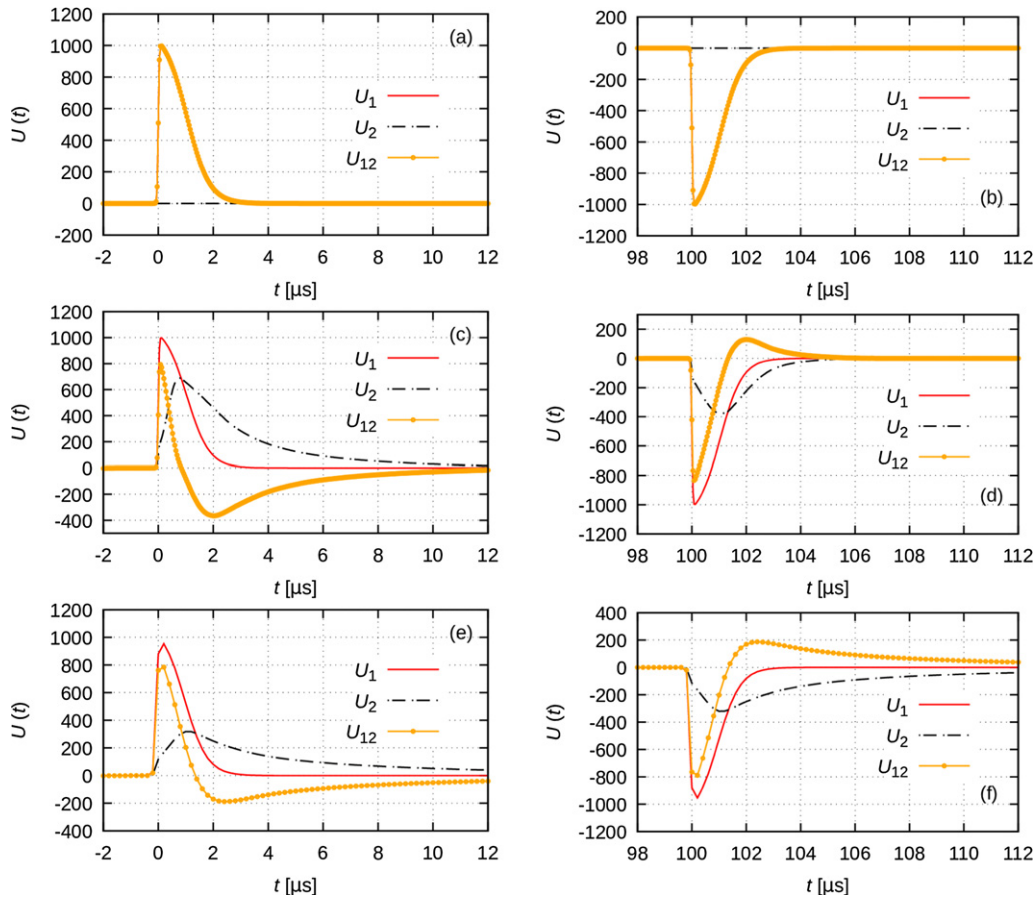


**Figure 2.** Time dependence of the potentials of the electrodes.  $U_1$  equals the applied voltage. In the case of a conducting grounded electrode  $U_2 = 0$ . If there is a dielectric layer on the grounded electrode,  $U_2$  is the surface potential.  $U_{12} = U_1 - U_2$  is the discharge voltage. The potentials are shown for (a), (b) both electrodes conducting, (c), (d) conducting powered electrode and dielectric layer on the grounded electrode, with  $\gamma_p = 0.07$  and  $\gamma_g = 0.3$ , (e), (f) the same as (c), (d) with  $\gamma_p = 0.07$  and  $\gamma_g = 0.07$ . Panels in the left column correspond to the positive polarity applied voltage pulses, while panels in the right column correspond to negative pulses. The peak value of the excitation is  $\hat{U}_1 = \pm 1000$  V,  $p = 100$  Pa, and  $L = 3$  cm.

Figures 2(a) and (b) show the case of a conducting grounded electrode. The potential of this electrode,  $U_2$ , is zero, and the voltage  $U_{12}$  over the discharge equals  $U_1$ , the potential applied to the powered electrode. Figures 2(c) and (d) depict the positive and negative pulses, respectively, for a grounded electrode with a dielectric surface. These results were obtained with  $\gamma_p = 0.07$  and  $\gamma_g = 0.3$ . Following the application of the high voltage pulses, the surface of the grounded electrode charges up in a way that the discharge voltage becomes lower in magnitude than the applied voltage. Beyond  $\approx 1.4 \mu\text{s}$  after the peaks of the excitation pulses  $|U_2|$  becomes higher than  $|U_1|$ , and consequently, the discharge voltage,  $U_{12}$ , changes sign. In the case of the positive excitation pulse, this ‘reversed voltage’ has a magnitude of about  $-400$  V, while for the negative pulse, it amounts about  $150$  V. This asymmetry originates from the different values of the secondary electron yields at the two electrodes. The symmetry of the discharge is re-established when equal  $\gamma$  values are used, as figures 2(e) and (f) show for a pair of conducting/dielectric electrodes with  $\gamma_p = \gamma_g = 0.07$ . Of course, the value for the dielectric surface is unrealistically low. It was assumed only to confirm the correctness of the simulations, which are supposed to give symmetric results

because the dielectrics is modelled as a capacitor that can reside anywhere in the electrical circuit.

Figure 3 shows the potential distribution in the discharge for both the cases of the conducting and dielectric grounded electrodes following the application of a positive excitation pulse. The curves marked as ‘max  $U_1$ ’ correspond to the time of the maximum applied voltage, and the other curves show the potential distributions  $10$  and  $80 \mu\text{s}$  later. At the maximum applied voltage we observe the sheath formation at the grounded electrode ( $x = 0$  cm). At this time, the plasma potential is a few volts higher (not visible in the figure) compared to the potential of the powered electrode. At later times, the plasma potential decreases. This decrease is faster in the case of the conducting electrode, where after  $10 \mu\text{s}$  we find a value of about  $5$  V, whereas the plasma potential is  $\sim 30$  V in the case of the dielectric electrode. Note, however, that in the dielectric case the sheath ‘moves’ to the powered electrode at this time. Even later, the potential drops to about  $3$  V, for both types of the electrodes. The resulting ambipolar electric field and potential drops near both electrodes retain the electrons in the (afterglow) plasma between the pulses, as well as accelerate the ions towards the electrodes to compensate for the flux of

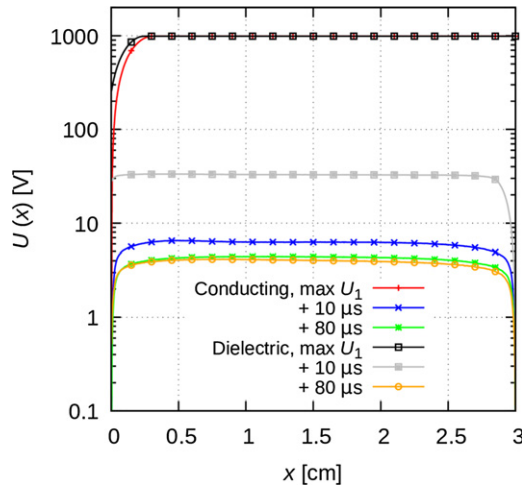


**Figure 3.** Potential distribution in the discharge for conducting and dielectric grounded electrodes, in the case of a positive excitation pulse. ‘max  $U_1$ ’ is the potential at the time of the maximum applied voltage, other curves show the potential distributions at later times specified in the legend. ‘Base case’ discharge conditions:  $\hat{U}_1 = 1000$  V,  $p = 100$  Pa. The grounded electrode is located at  $x = 0$  cm, while the powered electrode is at  $x = L = 3$  cm.

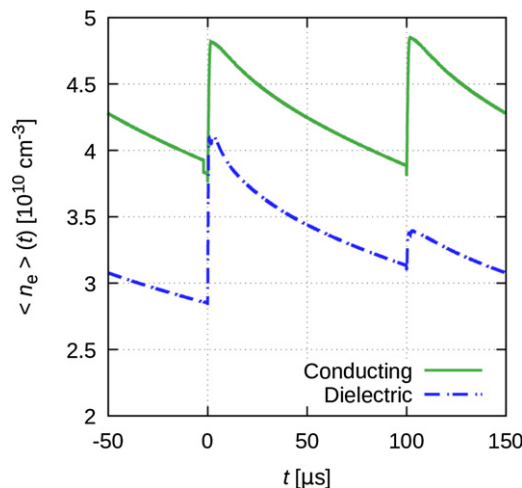


**Figure 4.** Time dependence of the spatially averaged electron density in the cases of conducting and dielectric grounded electrode. ‘Base case’ discharge conditions:  $\hat{U}_1 = 1000$  V,  $p = 100$  Pa, and  $L = 3$  cm.

fast electrons escaping from the plasma. The electric field near the electrode surfaces is in the order of  $\sim 80$  V cm $^{-1}$  during the late afterglow.

The markedly different behaviour of the gap voltage in the cases of a conducting vs. a dielectric grounded electrode, revealed in figure 2, has consequences on the charged particle dynamics and the discharge characteristics. For example, the temporal evolution of the mean (i.e. spatially averaged) electron density is significantly different in these two cases, as it can be seen in figure 4.

In the case of a conducting grounded electrode the average electron density varies between  $3.8 \times 10^{10}$  cm $^{-3}$  and  $4.8 \times 10^{10}$  cm $^{-3}$ , for the base conditions of  $\hat{U}_1 = 1000$  V,

$p = 100$  Pa, and  $L = 3$  cm. Upon the appearance of the excitation pulses a very sharp increase is observed, which is followed by a slow decay. The dynamics is the same for the positive and negative excitation pulses. Between the high-voltage excitation pulses the electron density is retained by the ambipolar electric field that builds up in the gap. At the relatively high pressure, a large amount of the charged particles survives in the gap between the excitation pulses.

For the dielectric grounded electrode, on the other hand, very different behaviour is found for the pulses with opposite polarity, which is a consequence of the different values of the secondary electron yields at both electrodes. The positive pulse results in an approximately four times higher ‘jump’ of the density as compared to that found for the negative pulse. This can be explained by the fact that upon the application of the positive pulse, the grounded electrode with the dielectric layer acts as the temporary cathode, where the charge reproduction mechanisms are largely enhanced due to the higher  $\gamma$ . In this case, the average electron density varies between  $2.8 \times 10^{10}$  cm $^{-3}$  and  $4.15 \times 10^{10}$  cm $^{-3}$ . Further information about the spatio-temporal behaviour of the electron density is revealed in figure 5.

In the case of conducting grounded electrode (see figure 5(a)) symmetrical patterns (mirrored in space and shifted in time) of the spatial distribution of the electron density can be observed. Upon the appearance of the excitation pulses a significant increase of the electron density occurs. The positive excitation pulse results in an electron density increase near the grounded electrode (situated at  $x/L = 0$ ), while the negative excitation pulse results in the buildup of high electron density near the powered electrode (situated at  $x/L = 1$ ), which act as the temporary cathode at the given times and voltage polarities. Following the termination of the excitation pulses the electron density spreads towards the centre of the discharge. In the case of the dielectric grounded electrode a remarkable asymmetry is observed between the negative and positive excitation pulses, as it can be seen in figure 5(b).

It is a peculiarity of the discharge with a dielectric electrode that an increase of the electron density is also observed at the anode side upon the application of the high-voltage pulses. Such an increase is not seen for the conducting grounded electrode, in figure 5(a). The reason for this is the reversed potential (c.f. figures 2(c) and (d)), the effect of which on the ionisation is studied in figure 6. The (a) and (b) panels of this figure show the ionisation source function,  $S_i(x, t)$ , for the conducting electrode, while panels (c) and (d) present the dielectric case.

In the case of the conducting grounded electrode, significant ionisation is observed during  $\approx 1.5$   $\mu$ s, i. e., close to the width of the excitation pulses. Ionisation is confined to within approximately one-fourth of the gap, in the vicinity of the temporary cathode.

For the dielectric grounded electrode, the ionisation is confined to a narrower time interval ( $\lesssim 0.8$   $\mu$ s), because the charging of the dielectrics leads to the self-termination of the discharge. Due to the appearance of a reversed potential over the electrode gap as a consequence of this charging process a weaker, but still significant ionisation is also observed at the ‘opposite’ electrode, as figures 6(c) and (d) reveal. Ionisation

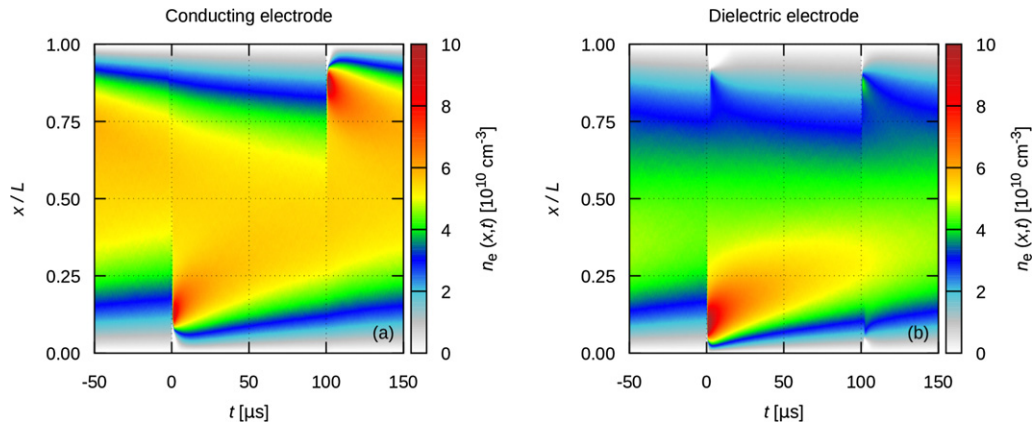


**Figure 5.** Spatio-temporal distribution of the electron density in the cases of (a) conducting and (b) dielectric grounded electrode. ‘Base case’ discharge conditions:  $\hat{U}_1 = 1000$  V,  $p = 100$  Pa, and  $L = 3$  cm. The grounded electrode is located at  $x/L = 0$ , while the powered electrode is at  $x/L = 1$ .

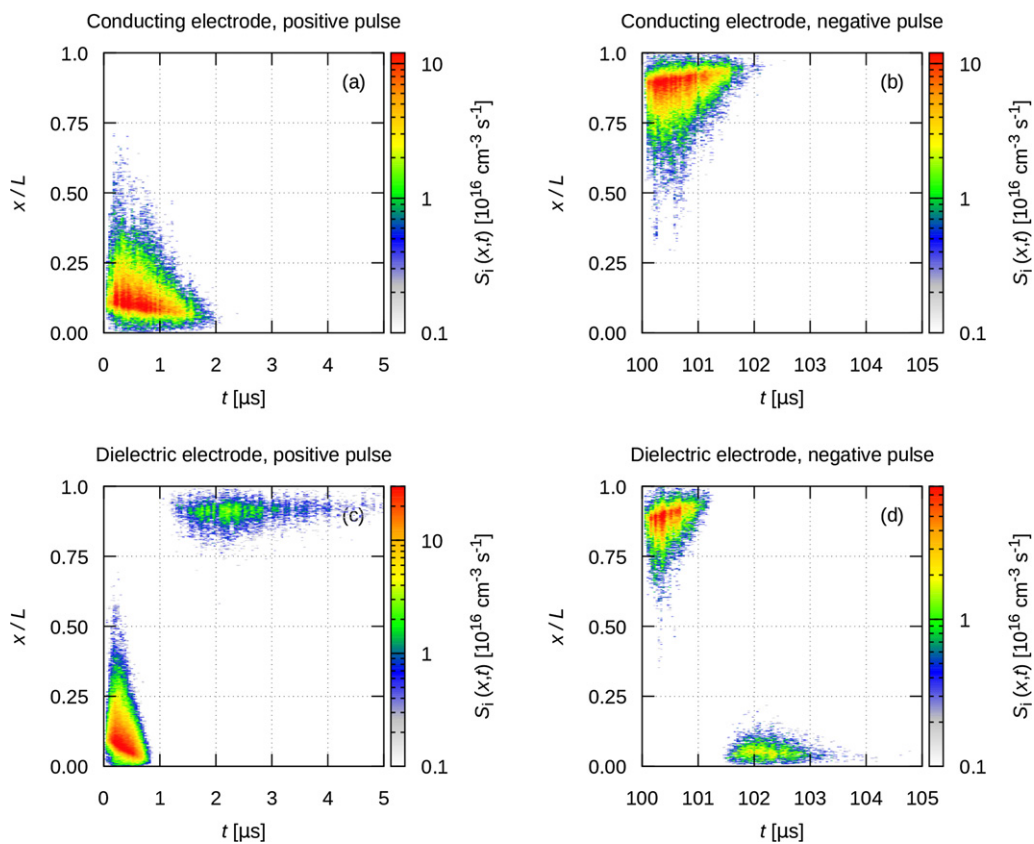


**Figure 6.** Spatio-temporal distribution of the ionisation source function,  $S_i(x, t)$ , in the case of (a), (b) conducting and (c), (d) dielectric grounded electrode. Panels in the left column correspond to the positive polarity applied voltage pulses, while panels in the right column correspond to negative pulses. ‘Base case’ discharge conditions:  $\hat{U}_1 = 1000$  V,  $p = 100$  Pa, and  $L = 3$  cm. The grounded electrode is located at  $x/L = 0$ , while the powered electrode is at  $x/L = 1$ .

in these domains of space and time is weaker compared to that caused by the primary pulse.

In plasma processing of materials, the energy distribution of the ions reaching the electrodes is very important. In the following, we examine the energy of the  $\text{Ar}^+$  ions at the grounded electrode. In the panels of figure 7, each arriving ion is represented by a dot. Panels (a) and (b) in the first row present the case of the conducting grounded electrode, within a time

‘window’ of  $10 \mu\text{s}$ . Due to the rapidly increasing voltage near  $t = 0 \mu\text{s}$ , the energy of the ions increases promptly and ions with up to  $\sim 500$  eV are found right after applying the positive excitation pulse. (Recall that in this case, the grounded electrode is the temporary cathode.) Streaming of the high-energy ions to the surface lasts for about  $2 \mu\text{s}$ . Subsequently, the energy of the ions falls below  $\sim 5$  eV. Low energy ions, accelerated by the ambipolar electric field, continue to stream



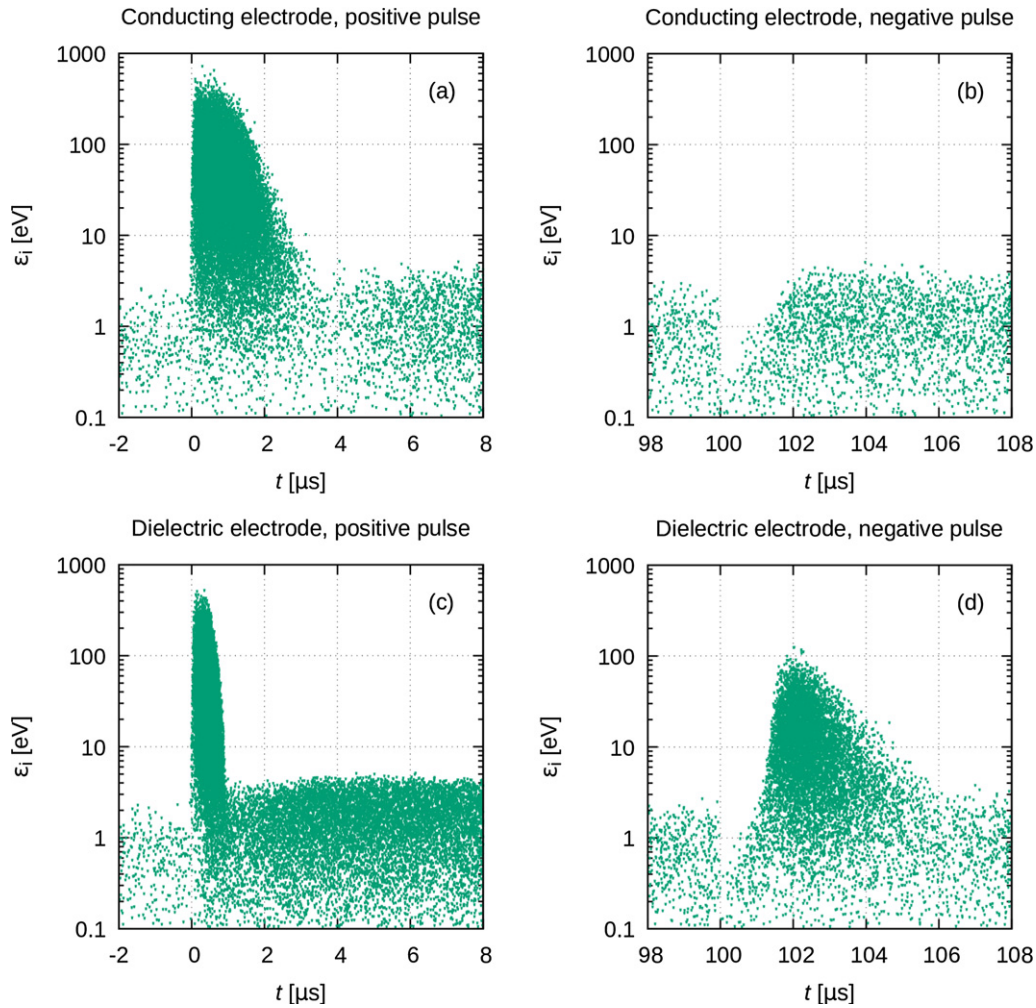


**Figure 7.** Energy of individual ions (represented as single dots) reaching the grounded electrode, in the case of a conducting (a), (b) and dielectric surface (c), (d). Panels (a) and (c) refer to the vicinity of the positive excitation pulse, while (b) and (d) show the distributions in the vicinity of the negative excitation pulse. ‘Base case’ discharge conditions:  $\hat{U}_1 = 1000$  V,  $p = 100$  Pa, and  $L = 3$  cm.

to the electrode until the second excitation pulse with negative polarity arrives at  $t = 100 \mu\text{s}$ . Upon the arrival of the negative excitation pulse the ion energy and the number of incoming ions are slightly depleted at the grounded electrode because it acts as the temporary anode. A few  $\mu\text{s}$  later the low energy  $\text{Ar}^+$  ion flow to the electrode is re-established.

In the case of the dielectric grounded electrode, the pulse of the high-energy ions due to the positive excitation pulse (figure 7(c)) lasts for a shorter time as compared to the conducting grounded electrode case. Here, the ions reach about the same energy but their flux (proportional to the density of dots in the representation used in figure 7) after the excitation pulse is much higher compared to the conducting case. At the time of the negative excitation pulse (see figure 7(d)), the ion energy and flux are first depleted similarly to the case of the conducting electrode. However, a bunch of high-energy ions is observed following the negative voltage pulse, as expected under the reversal of the gap voltage (discussed earlier).

The flux and the mean energy of  $\text{Ar}^+$  ions for the conducting and dielectric grounded electrodes are shown in

figures 8(a) and (b), respectively. In both cases, the ion fluxes are in the order of  $10^{15} \text{ cm}^{-2} \text{ s}^{-1}$ , and the mean ion energy approaches 100 eV upon the application of the positive excitation pulses. This value drops to  $\lesssim 1$  eV between the excitation pulses.

The energy of the ions arriving during the afterglow periods to the electrodes is determined by the strength of the ambipolar electric field discussed in relation to figure 3. The cross section for the  $\text{Ar}^+ + \text{Ar}$  collisions at low ion energies is about  $\sigma_i \approx 5 \times 10^{-15} \text{ cm}^2$  [95]. At the given values of the gas pressure and temperature, the gas density is  $n_g \approx 2.1 \times 10^{16} \text{ cm}^{-3}$ . At these values the free path of the ions is in the order of 0.01 cm. The ambipolar electric field of  $\sim 80 \text{ V cm}^{-1}$  found for the base conditions near the electrode surfaces results in the mean ion energy of  $\approx 0.8$  eV in between the pulses, and this is clearly the value that we observe in figure 8.

### 3.2. Effects of the operating conditions

In this section, we present simulation results for the time-dependence of the mean electron density, as well as for the flux and the mean energy of the  $\text{Ar}^+$  ions streaming to the grounded

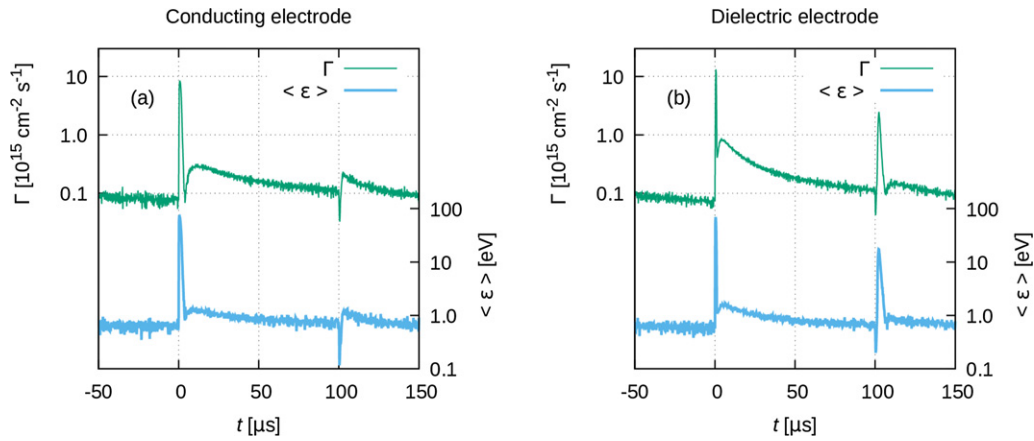


**Figure 8.** Flux and mean energy of  $\text{Ar}^+$  ions reaching the grounded electrode as a function of time. The grounded electrode had either conducting (a) or dielectric (b) surface.

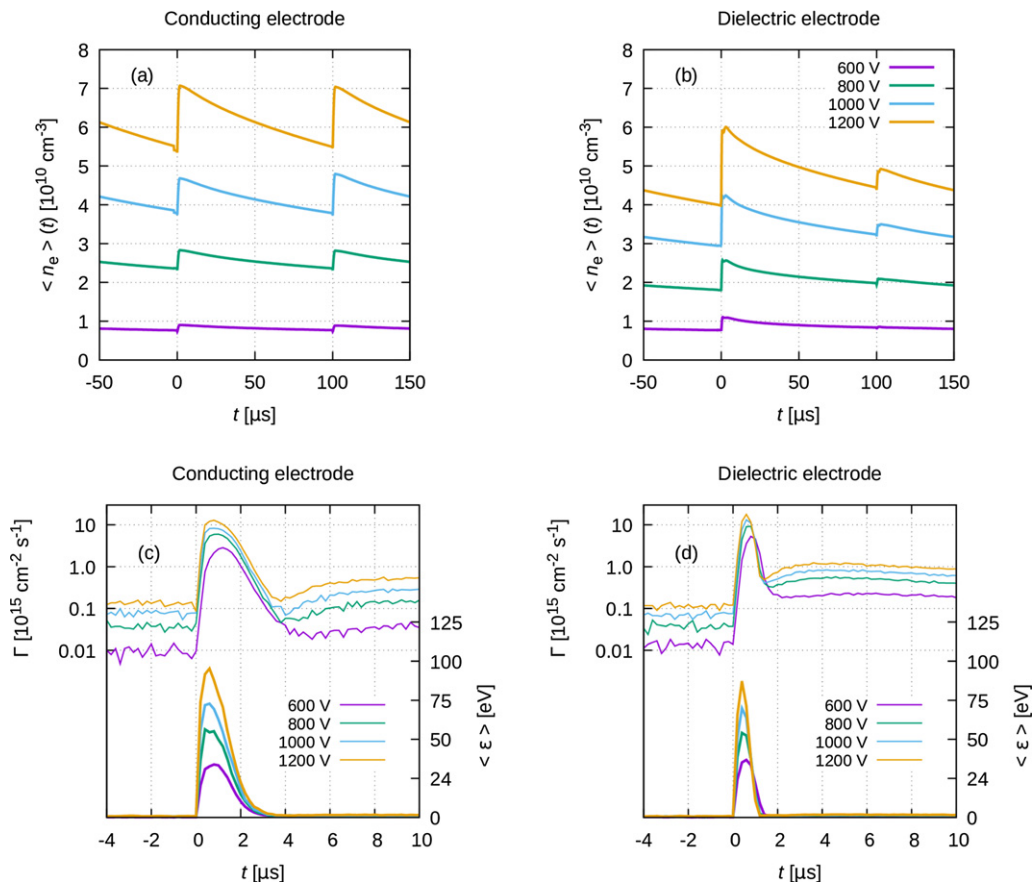


**Figure 9.** Effect of the driving voltage pulse amplitude on the discharge characteristics: (a), (b) mean electron density as a function of time; (c), (d) flux (left scale, upper set of thin lines) and mean energy (right scale, lower set of thick lines) of  $\text{Ar}^+$  ions reaching the grounded electrode as a function of time. Results for the case of a conducting grounded electrode are shown in the left column, while results for the case of a dielectric electrode are shown in the right column.  $p = 100$  Pa,  $L = 3$  cm,  $\gamma = 0.07$  for the conducting surfaces and  $\gamma = 0.3$  for the dielectric surface.

electrode of the discharge, as a function of the excitation voltage pulse amplitude, the gas pressure, and the electrode gap.

Figure 9 presents the simulation results for different driving voltage peak amplitudes, at fixed gas pressure and electrode separation ( $p = 100$  Pa and  $L = 3$  cm). Panels

(a), (c), (b) and (d), respectively, refer to the cases of the conducting and dielectric grounded electrode. As it can be seen in panel (a), the electron density increases significantly with the voltage pulse amplitude. Doubled voltage pulse amplitude results in seven times increased electron density. The increase of the density upon the application of the excitation

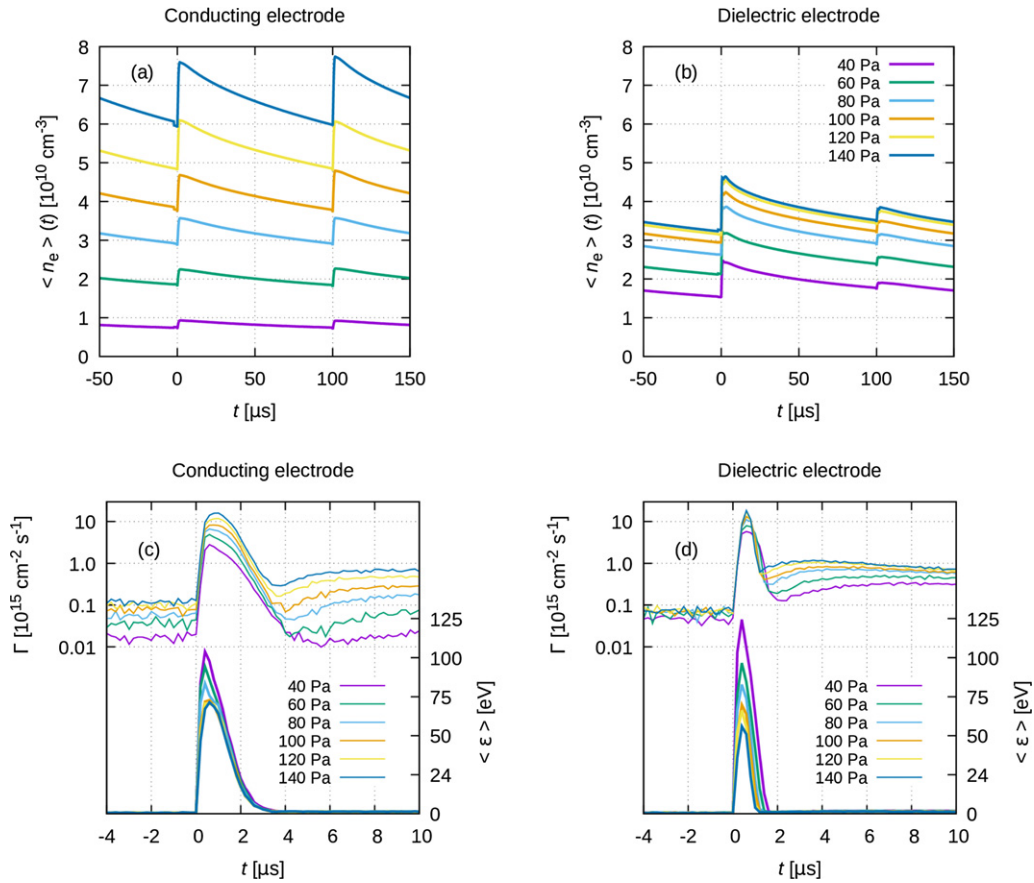


**Figure 10.** Effect of the gas pressure on the discharge characteristics: (a), (b) mean electron density as a function of time; (c), (d) flux (left scale, upper set of thin lines) and mean energy (right scale, lower set of thick lines) of  $\text{Ar}^+$  ions reaching the grounded electrode as a function of time. Results for the case of a conducting grounded electrode are shown in the left column, while results for the case of a dielectric electrode are shown in the right column.  $U_1 = 1000$  V,  $L = 3$  cm,  $\gamma = 0.07$  for the conducting surfaces and  $\gamma = 0.3$  for the dielectric surface.

(i.e., the time-modulation of the mean electron density) is also more pronounced at higher voltage peak amplitudes due to more efficient electron multiplication in the avalanches near the temporary cathode.

For the grounded electrode covered by a dielectric layer, the electron density is generally lower as compared to the case of the conducting electrode (figure 9(b)). The reason for this has already been discussed in section 3.1. The charging of the dielectric surface decreases the efficiency of the power coupling into the plasma due to the decrease of the gap voltage (cf. the discussion related to figure 2), despite the higher secondary electron yield of the dielectric surface. We recall that the uneven increase of the density upon the application of the positive and negative pulses (at  $t = 0$   $\mu\text{s}$ , and  $100$   $\mu\text{s}$ , respectively) is the consequence the different secondary electron emission coefficients adopted for conducting and dielectric surfaces. The mean ion energy during the application of the high-voltage pulses scales nearly linearly with the voltage amplitude, as it can be seen in figures 9(c) and (d). The peak values of the ion flux are comparable in the cases of conducting and dielectric grounded electrode surfaces, and both exhibit an increase at higher voltages.

The effect of the gas pressure is revealed in figure 10. For the case of a conducting grounded electrode we observe

a nearly linear increase of the mean electron density with increasing gas pressure (see figure 10(a)). In the case of a dielectric grounded electrode, a much less significant increase is observed (see figure 10(b)). It can be explained by the different ‘charging rates’ of the dielectric surface of the grounded electrode as a function of the plasma density. We can follow the effect with the aid of figure 11 showing the time-dependence of the potentials of the electrodes and the gap voltage ( $U_{12}$ ) for different gas pressures between 40 Pa and 140 Pa. While at the lowest pressure the potential at the dielectric surface rises up to  $\approx 440$  V, at 80 Pa this value grows to 600 V, and at 140 Pa to about 750 V. This increase of the surface potential effectively decreases the gap voltage, and the shortening of the positive ‘wave’ of  $U_{12}$  with increasing pressure becomes more significant. It limits the electron density that can be reached at a given voltage.

The peak value of the ion flux at the grounded electrode increases nearly linearly with the gas pressure in the case of a conducting grounded electrode, following the behaviour of the electron density (which is nearly the same as the ion density in the bulk plasma), see figures 10(a) and (c). In the case of a dielectric surface, the ion flux saturates with the increase of the pressure due to the reasons discussed above. Lower pressure result in higher ion energies due to a longer ion mean free path



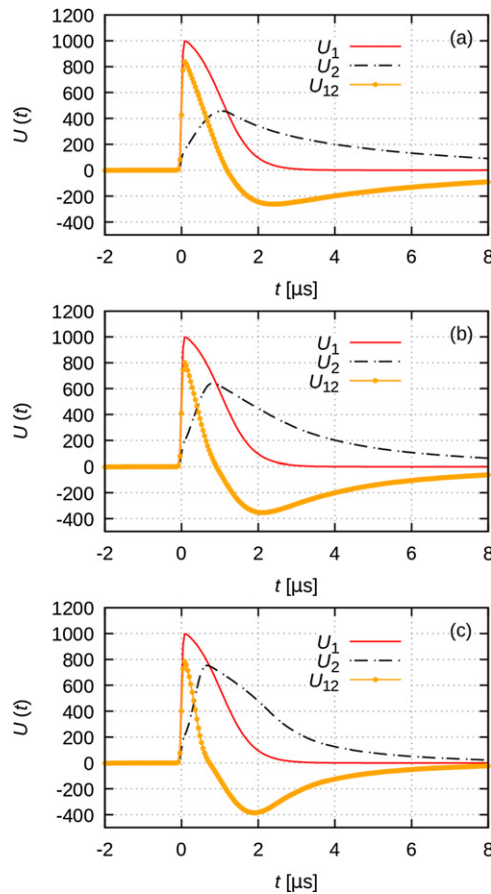


**Figure 11.** Time dependence of the potentials of the electrodes.  $U_1$  equals the applied voltage,  $U_2$  is the surface potential of the dielectric at the grounded electrode,  $U_{12} = U_1 - U_2$  is the discharge voltage. (a) 40 Pa, (b) 80 Pa, and (c) 140 Pa.  $\tilde{U}_1 = 1000$  V,  $L = 3$  cm.

within the sheath region where a high electric field is present at times of high discharge voltage (see figures 10(b) and (d)).

The effects of the electrode gap ( $L$ ) on the discharge characteristics (at a fixed voltage pulse amplitude of 1000 V and a gas pressure of 100 Pa) is demonstrated in figure 12. We observe a significant increase of the mean (spatially averaged) electron density with decreasing electrode gap. At a fixed pressure we expect that roughly the same number of electrons is created in the discharge pulses and the peak of the spatio-temporal distribution of the electrons is similar for different values of the gap. As the spatial average of the electron density at a larger  $L$  is taken over a higher volume a lower  $\langle n_e \rangle$  is obtained at a bigger gap. Due to a faster diffusion decay a shorter gap results in a somewhat lower  $\langle n_e \rangle L$  product.

### 3.3. Comparison with experiments

The simulation parameters employed in this study were inspired by recent plasma polymerization and surface treatment experiments carried out in high voltage bipolar-pulsed discharges [85, 86]. However, no detailed plasma diagnostics have been performed for such plasmas yet. An earlier study [90] presented the electron temperatures and densities obtained from Langmuir probe measurements at the center

between the two electrodes in a similar parallel-plate high-voltage pulsed discharge system. In this experiment, the two parallel electrodes were made of Cu, i.e., both metallic, as sketched in figure 1(a). The electrodes had a diameter of 6 cm and the gap between the electrodes was 3 cm. The discharge was ignited in Ar at the pressure of 100 Pa using monopolar voltage pulses with peak values of  $-350$  V  $\sim$   $-650$  V applied for a duration of  $20$   $\mu$ s each. The interval between two consecutive pulses was 1 ms, i.e., the duty cycle was 2%.

For a comparison between the experiment and simulation, we take a  $-600$  V pulse amplitude as a test case. For this case, the electron density at the middle of the electrode gap after the termination of the excitation pulses was found to be  $4.5 \times 10^{10}$   $\text{cm}^{-3}$  in the experiment (see figure 3(b) of [90]). Our numerical simulation under the same conditions (figure 13) shows that the electron density at the center reaches a very similar value after the termination of the excitation pulse. However, in the experiment this density was measured at  $5$   $\mu$ s after the termination of the excitation, while the simulation gives this density at somewhat later time (at about  $50$   $\mu$ s). The different time-dependence that we observe may be due to uncertainties in the secondary electron emission coefficient and the pulse shapes in the experiment vs. the simulation, as well as due to the uncertainty of the probe measurements. The experiments and the simulations, on the other hand, both show (in agreement) that the central density hardly changes for a few hundred  $\mu$ s after the pulse. The agreement between the experimental and simulation data shown here indicates that our simulations presented in earlier subsections also reproduce corresponding discharge phenomena in experiments reasonably well.

Our study shows that, even at a duty cycle of 1%, a plasma with a density of  $1 \sim 5 \times 10^{15}$   $\text{cm}^{-3}$  remains in the original discharge region under the typical conditions that we examined in this study for pulsed Ar discharges. As seen in figure 8, more than a half of the total ion dose arrives at the surface during the off-pulse period. Figure 7 shows that energetic ion bombardment with an ion energy of several hundred eV is restricted to a short period of approximately  $2$   $\mu$ s during and after the high voltage application. In plasma polymerization experiments using a pulsed plasma system with a gas containing deposition precursors, our Ar-based simulation results also indicate that the deposition of polymer precursors, which are considered to be primarily charge-neutral radicals, are likely to occur continuously when a low-density plasma remains in the discharge chamber. On the other hand, the energetic ion bombardment for the very short period of time may cause cross linking of the deposited polymer in addition to sputtering. Since the pulse duty cycle is 1%, sputtered polymer fragments may return to the surface and redeposit. The periodic ion bombardment may also cause the surface chemical reactions that determine the surface chemical compositions. For example, in the case of amine-rich polymer formation [85, 86], the formation of primary and secondary amine groups in the polymerized film is known to be influenced by not only the influx of amine containing precursors but also ion bombardment that can breakup deposited amine groups. The typical power consumption of the plasma system obtained from



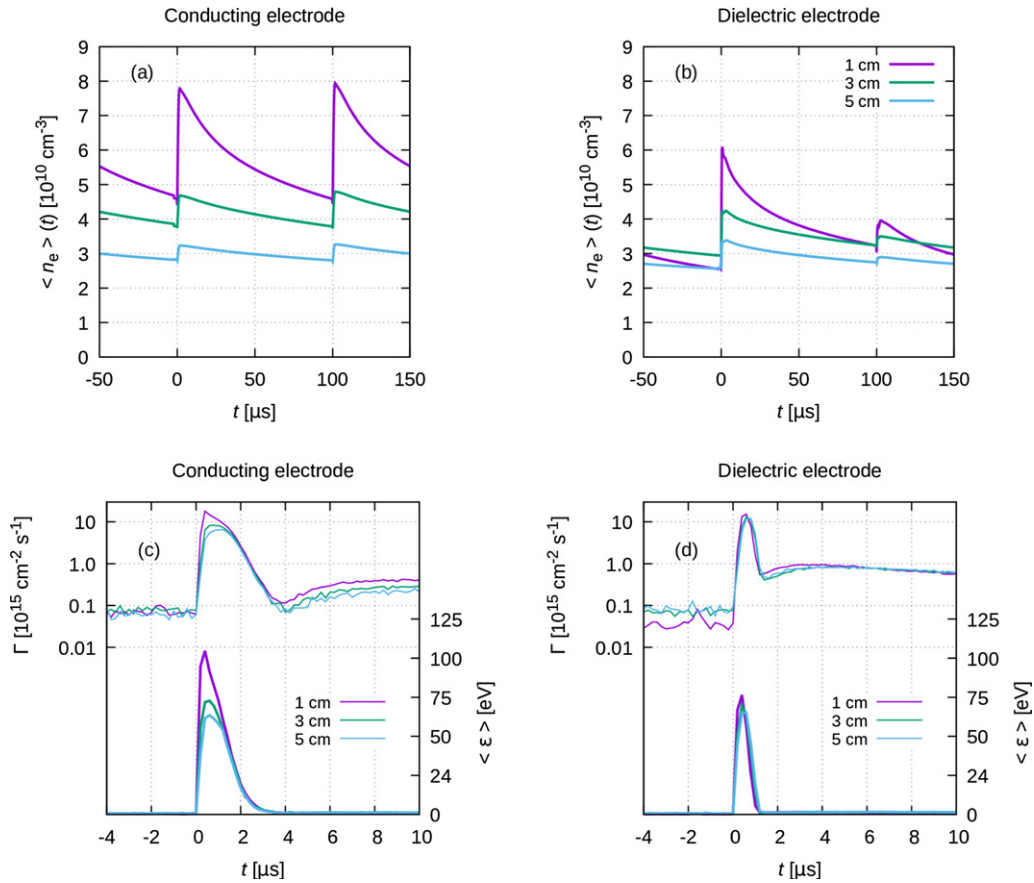


**Figure 12.** Effect of the electrode gap on the discharge characteristics: (a), (b) mean electron density as a function of time; (c), (d) flux (left scale, upper set of thin lines) and mean energy (right scale, lower set of thick lines) of  $\text{Ar}^+$  ions reaching the grounded electrode as a function of time. Results for the case of a conducting grounded electrode are shown in the left column, while results for the case of a dielectric electrode are in the right column.  $\hat{U} = 1000$  V,  $p = 100$  Pa,  $\gamma = 0.07$  for the conducting surfaces and  $\gamma = 0.3$  for the dielectric surface.

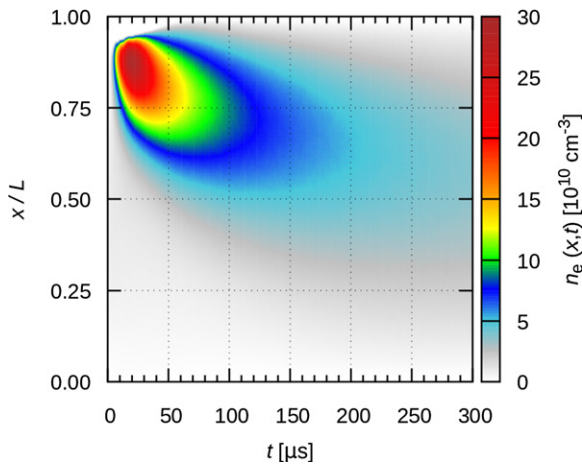


**Figure 13.** Spatio-temporal distribution of the electron density for the case of an unipolar voltage pulse with  $-600$  V amplitude and  $20$   $\mu\text{s}$  duration. The repetition rate is  $1$  ms (the figure shows only a part of this period),  $p = 100$  Pa,  $L = 3$  cm, and  $\gamma = 0.07$ . The metal grounded electrode is located at  $x/L = 0$ , while the metal powered electrode is at  $x/L = 1$ .

the simulation is in the order of  $10 \text{ mW cm}^{-2}$  on time average. Therefore, for a typical plasma system with an electrode of  $20$  cm diameter, the total power consumption would be a

few W. Considering the sufficient heat conduction through the metallic parts used in such a plasma system, we expect that the surface temperature remains close to room temperature. Together, the simulation results clearly indicate that a low-duty-cycle high-voltage pulsed plasma discharge can provide an ideal environment for plasma polymerization with low surface temperature and high surface chemical reactivities.

#### 4. Summary

We have presented a numerical simulation study of a high voltage gas discharge, excited by microsecond pulses with alternating polarity and having a low duty cycle of approximately 1%. Our studies have considered a parallel plate electrode configuration with a powered electrode made of conducting material and a grounded electrode with a conducting or a dielectric surface. The plasma source has been described using the particle-in-cell approach combined with the Monte Carlo treatment collision processes.

A detailed analysis of the discharge was presented for a ‘base’ set of conditions:  $1000$  V voltage pulse amplitude,  $100$  Pa pressure and  $3$  cm electrode gap. The computed space- and time-resolved ionisation source function and electron density distribution provided detailed insight into the plasma formation. Tracing the ions in the simulations made it possible to

derive the time dependence of their flux and the mean energy at the electrode surfaces. Despite the relatively high pressures considered here, it was found that the ion energies reach several hundreds of electron volts. In the case of a dielectric-covered electrode, the plasma density and the ion flux to the electrodes were found to be self-limited as a function of the pressure, within the parameter range considered.

The energy distribution and the flux of the ions computed at numerous combinations of the external control parameters (voltage pulse amplitude, gas pressure and electrode gap) may aid the optimisation of the surface treatment applications of this type of plasma sources.

In our model we did not take into account the effect of the metastable atoms on the discharges. Considering the relatively high gas pressures and the low electron energy between the excitation pulses, processes like stepwise ionisation from Ar metastable and resonant states [99, 100] can contribute significantly to charged particle production. Extension of the model in this direction is foreseen to be possible, however, this is left for future work. We have also disregarded the sputtering of the electrodes due to ion bombardment as a result of which a certain amount of metal can be present in the plasma. Based on the sputtering yield of Ar<sup>+</sup> ions for stainless steel electrodes (computed according to [101]) we estimate the ratio of the fluxes of the sputtered metal and the sputtering Ar<sup>+</sup> ions at the electrodes to be in the range of few percent for the conditions studied. Therefore, we do not expect that a significant metal vapour density establishes in the plasma. This conclusion may change when an electrode material with higher sputtering rate is considered (e.g. Cu) and/or when higher voltages are used in conjunction with lower gas pressures.

## Acknowledgments

This work was supported by the National Office for Research, Development and Innovation (NKFIH) of Hungary via Grant 119357, Osaka University International Joint Research Promotion Programs (Type A and Type B), Japan Society of the Promotion of Science (JSPS) Grant-in-Aid for Scientific Research(S) 15H05736, and JSPS Core-to-Core Program JPJSCCA2019002. AAH is also grateful for the financial support by Research and Innovation in Science and Technology Project (RISET-PRO), Ministry of Research, Technology, and Higher Education of Indonesia. LZ is grateful to the Czech Science Foundation project 18-12774S and to the Ministry of Education, Youth and Sports of the Czech Republic supporting the project CEITEC 2020 (LQ1601).

## ORCID iDs

Zoltán Donkó  <https://orcid.org/0000-0003-1369-6150>  
 Lenka Zajíčková  <https://orcid.org/0000-0002-6906-8906>  
 Anjar Anggraini Harumningtyas  <https://orcid.org/0000-0002-1593-6851>  
 Satoshi Hamaguchi  <https://orcid.org/0000-0001-6580-8797>

## References

- [1] Coburn J W and Winters H F 1983 *Annu. Rev. Mater. Sci.* **13** 91
- [2] Graves D B 1994 *IEEE Trans. Plasma Sci.* **22** 31
- [3] Lieberman M A and Lichtenberg A J 1994 *Principles of Plasma Discharges and Processing* (New York: Wiley)
- [4] Hamaguchi S and Rossnagel S M 1996 *J. Vac. Sci. Technol. B* **14** 2603
- [5] Mayo A A, Hamaguchi S, Joo J H and Rossnagel S M 1997 *J. Vac. Sci. Technol. B* **15** 1788
- [6] Hamaguchi S 1999 *IBM J. Res. Dev.* **43** 199
- [7] Chen F F and Chang J P 2003 *Lecture Notes on Principles of Plasma Processing* (Berlin: Springer)
- [8] Rath J 2003 *Sol. Energy Mater. Sol. Cells* **76** 431
- [9] Yamada H and Hamaguchi S 2004 *J. Appl. Phys.* **96** 6147
- [10] Makabe T and Petrović Z 2006 *Plasma Electronics (Applications in Microelectronic Device Fabrication)* (London: Taylor and Francis)
- [11] Taguchi M and Hamaguchi S 2007 *Thin Solid Films* **515** 4879
- [12] Donnelly V M and Kornblit A 2013 *J. Vac. Sci. Technol., A* **31** 050825
- [13] Chu P K, Chen J Y, Wang L P and Huang N 2002 *Mater. Sci. Eng.* **36** 143
- [14] Gomathi N, Sureshkumar A and Neogi S 2008 *Curr. Sci.* **94** 1478 <https://www.jstor.org/stable/24100504>
- [15] Fridman A and Friedman G 2013 *Plasma Medicine* (New York: Wiley)
- [16] Oehrlein G S and Hamaguchi S 2018 *Plasma Sources Sci. Technol.* **27** 023001
- [17] Weltmann K D et al 2019 *Plasma Process. Polym.* **16** 1800118
- [18] Ohta H and Hamaguchi S 2001 *J. Vac. Sci. Technol., A* **19** 2373
- [19] Karahashi K and Hamaguchi S 2014 *J. Phys. D: Appl. Phys.* **47** 224008
- [20] Ito T, Karahashi K, Fukasawa M, Tatsumi T and Hamaguchi S 2011 *J. Vac. Sci. Technol., A* **29** 050601
- [21] Ito T, Karahashi K, Fukasawa M, Tatsumi T and Hamaguchi S 2011 *Jpn. J. Appl. Phys.* **50** 08KD02
- [22] Murakami Y, Horiguchi S and Hamaguchi S 2010 *Phys. Rev. E* **81** 041602
- [23] Micheltore A, Whittle J D and Short R 2015 *Front. Phys.* **3** 3
- [24] Hegemann D, Michlíček M, Blanchard N E, Schütz U, Lohmann D, Vandenbossche M, Zajíčková L and Drábik M 2016 *Plasma Process. Polym.* **13** 279
- [25] Akhavan B et al 2019 *Applied Materials Today* **16** 456
- [26] Heil B G, Czarnetzki U, Brinkmann R P and Mussenbrock T 2008 *J. Phys. D: Appl. Phys.* **41** 165202
- [27] Schuengel E, Donkó Z, Hartmann P, Derzsi A, Korolov I and Schulze J 2015 *Plasma Sources Sci. Technol.* **24** 045013
- [28] Lafleur T 2015 *Plasma Sources Sci. Technol.* **25** 013001
- [29] Delattre P-A, Lafleur T, Johnson E and Booth J-P 2013 *J. Phys. D: Appl. Phys.* **46** 235201
- [30] Donkó Z, Derzsi A, Vass M, Schulze J, Schuengel E and Hamaguchi S 2018 *Plasma Sources Sci. Technol.* **27** 104008
- [31] Derzsi A, Bruneau B, Gibson A R, Johnson E, O'Connell D, Gans T, Booth J-P and Donkó Z 2017 *Plasma Sources Sci. Technol.* **26** 034002
- [32] Zhang Y, Zafar A, Coumou D J, Shannon S C and Kushner M J 2015 *J. Appl. Phys.* **117** 233302
- [33] Coumou D J, Clark D H, Kummerer T, Hopkins M, Sullivan D and Shannon S 2014 *IEEE Trans. Plasma Sci.* **42** 1880
- [34] Diomede P, Economou D J, Lafleur T, Booth J-P and Longo S 2014 *Plasma Sources Sci. Technol.* **23** 065049
- [35] Brandt S, Berger B, Donkó Z, Derzsi A, Schüngel E, Koepke M and Schulze J 2019 *Plasma Sources Sci. Technol.* **28** 095021
- [36] Gibson A R et al 2019 *Plasma Sources Sci. Technol.* **28** 01LT01

- [37] Korolov I, Donkó Z, Hübner G, Bischoff L, Hartmann P, Gans T, Liu Y, Mussenbrock T and Schulze J 2019 *Plasma Sources Sci. Technol.* **28** 094001
- [38] Lundin D, Gudmundsson J T and Minea T 2019 *High Power Impulse Magnetron Sputtering (Fundamentals, Technologies, Challenges and Applications)* (Amsterdam: Elsevier)
- [39] Anders A 2017 *J. Appl. Phys.* **121** 171101
- [40] Little C E 1999 *Metal Vapour Lasers (Physics, Engineering and Applications)* (New York: Wiley)
- [41] Rocca J J, Shlyaptsev V, Tomasel F G, Cortázar O D, Hartshorn D and Chilla J L A 1994 *Phys. Rev. Lett.* **73** 2192
- [42] Kukhlevsky S V 2001 *Europhys. Lett.* **55** 660
- [43] Massines F, Gherardi N, Naudé N and Ségur P 2005 *Plasma Phys. Control. Fusion* **47** B577
- [44] Boeuf J P and Pitchford L C 2005 *J. Appl. Phys.* **97** 103307
- [45] Offerhaus B, Lackmann J-W, Kogelheide F, Bracht V, Smith R, Bibinov N, Stapelmann K and Awakowicz P 2017 *Plasma Process. Polym.* **14** 1600255
- [46] Pai D Z, Stancu G D, Lacoste D A and Laux C O 2009 *Plasma Sources Sci. Technol.* **18** 045030
- [47] Ibuka S, Mikami R, Furuya F, Ogura K, Yasuoka K and Ishii S 2007 *IEEE Trans. F.M.* **127** 411
- [48] Iza F, Walsh J L and Kong M G 2009 *IEEE Trans. Plasma Sci.* **37** 1289
- [49] Lo C-W and Hamaguchi S 2011 *J. Phys. D: Appl. Phys.* **44** 375201
- [50] Ito T, Kanazawa T and Hamaguchi S 2011 *Phys. Rev. Lett.* **107** 065002
- [51] Huang B-D, Takashima K, Zhu X-M and Pu Y-K 2015 *J. Phys. D: Appl. Phys.* **48** 125202
- [52] Roettgen A, Shkurenkov I, Simeni Simeni M, Adamovich I V and Lempert W R 2016 *Plasma Sources Sci. Technol.* **25** 055008
- [53] Machala Z, Pai D Z, Janda M and Laux C O 2014 *Atmospheric pressure nanosecond pulsed discharge plasmas Low Temperature Plasma Technology: Methods and Applications* ed P K Chu and X P Lu (Boca Raton, FL: CRC Press)
- [54] Schregel C-G, Carbone E A D, Luggenhölscher D and Czarnetzki U 2016 *Plasma Sources Sci. Technol.* **25** 054003
- [55] Song S, Lane J and Jiang C 2018 *IEEE Trans. Plasma Sci.* **46** 587
- [56] Donkó Z, Hamaguchi S and Gans T 2018 *Plasma Sources Sci. Technol.* **27** 054001
- [57] Donkó Z, Hamaguchi S and Gans T 2019 *Plasma Sources Sci. Technol.* **28** 075004
- [58] Starikovskaia S M, Kukaev E N, Kuksin A Y, Nudnova M M and Starikovskii A Y 2004 *Combust. Flame* **139** 177
- [59] Aleksandrov N L, Kindysheva S V, Kukaev E N, Starikovskaya S M and Starikovskii A Y 2009 *Plasma Phys. Rep.* **35** 867
- [60] Correale G, Popov I B, Ratik A E, Starikovskii A Y, Hulshoff S J and Veldhuis L L M 2011 *49th AIAA Aerospace Sciences Meeting AIAA 2011-1079*
- [61] Unfer T and Boeuf J P 2009 *J. Phys. D: Appl. Phys.* **42** 194017
- [62] Bokhan P A, Gugin P P, Zakrevsky D E and Lavrukhin M A 2013 *J. Phys. D: Appl. Phys.* **49** 245202
- [63] Bokhan P A, Gugin P P, Zakrevsky D E and Lavrukhin M A 2016 *Tech. Phys. Lett.* **42** 372
- [64] Zhou W, Li K, Li X, Qian H, Shao J, Fang X, Xie P and Liu W 2011 *Opt. Lett.* **36** 2961
- [65] Zhou W, Li K, Qian H, Ren Z and Yu Y 2012 *Appl. Optic.* **51** B42
- [66] Yumii T, Kimura N and Hamaguchi S 2013 *J. Appl. Phys.* **113** 213101
- [67] Yumii T, Yoshida T, Doi K, Kimura N and Hamaguchi S 2013 *J. Phys. D: Appl. Phys.* **46** 135202
- [68] Pai D Z 2011 *J. Phys. D: Appl. Phys.* **44** 174024
- [69] Scapinello M, Martini L M, Dilecce G and Tosi P 2016 *J. Phys. D: Appl. Phys.* **49** 075602
- [70] Lotfalipour R, Ghorbanzadeh A M and Mahdian A 2014 *J. Phys. D: Appl. Phys.* **47** 365201
- [71] Beebe S J, Fox P M, Rec L J, Somers K, Stark R H and Schoenbach K H 2002 *IEEE Trans. Plasma Sci.* **30** 286
- [72] Ayan H, Staack D, Fridman G, Gutsol A, Mukhin Y, Starikovskii A, Fridman A and Friedman G 2009 *J. Phys. D: Appl. Phys.* **42** 125202
- [73] Ikawa S, Kitano K and Hamaguchi S 2010 *Plasma Process. Polym.* **7** 33
- [74] Miura T, Ando A, Hirano K, Ogura C, Kanazawa T, Ikeguchi M, Seki A, Nishihara S and Hamaguchi S 2014 *J. Phys. D: Appl. Phys.* **47** 445402
- [75] Ito T, Gotoh K, Sekimoto K and Hamaguchi S 2015 *Plasma Med.* **5** 283
- [76] Miura T, Hamaguchi S and Nishihara S 2016 *J. Phys. D: Appl. Phys.* **49** 165401
- [77] Weltmann K D, Polak M, Masur K, von Woedtke T, Winter J and Reuter S 2010 *Contrib. Plasma Phys.* **52** 644
- [78] Stoffels E 2002 *High Temperature Material Processes (An International Quarterly of High-Technology Plasma Processes)* vol 6 (Danbury, CT: Begell House) p 1093
- [79] Mändl S, Sader R, Thorwarth G, Krause D, Zeilhofer H-F, Horch H H and Rauschenbach B 2002 *Biomol. Eng.* **19** 129
- [80] Chu P K 2007 *Surf. Coat. Technol.* **201** 5601
- [81] Solovieva A et al 2017 *Polym.* **9** 736
- [82] Ding C X, Xue W C, Liu X Y and Zheng X B 2004 *Chin. J. Nonferrous Metals* **14** 306
- [83] Lee D-S, Moriguchi Y, Okada K, Myoui A, Yoshikawa H and Hamaguchi S 2011 *IEEE Trans. Plasma Sci.* **39** 2166–7
- [84] Moriguchi Y, Lee D-S, Chijimatsu R, Thamina K, Masuda K, Itsuki D, Yoshikawa H, Hamaguchi S and Myoui A 2018 *PLoS One* **13** e0194303
- [85] Harumningtyas A A et al 2019 *Proc. of Int. Symp. on Plasma Chemistry (ISPC)*
- [86] Michlicek M, Hamaguchi S and Zajickova L 2020 *Plasma Sources Sci. Technol.* submitted <https://doi.org/10.1088/1361-6595/abb2e8>
- [87] Murakami N, Tanaka K, Sugimoto S, Kiuchi M and Goto S 2001 *Surf. Coat. Technol.* **136** 265
- [88] Kiuchi M, Murai K, Tanaka K, Takechi S, Sugimoto S and Goto S 2001 *Surf. Coat. Technol.* **136** 273
- [89] Sugimoto S, Kiuchi M, Takechi S, Tanaka K and Goto S 2001 *Surf. Coat. Technol.* **136** 65
- [90] Takechi S, Sugimoto S, Kiuchi M, Tanaka K and Goto S 2001 *Surf. Coat. Technol.* **136** 69
- [91] Birdsall C K 1991 *IEEE Trans. Plasma Sci.* **19** 65
- [92] Verboncoeur J P 2005 *Plasma Phys. Control. Fusion* **47** A231
- [93] Matyash K, Schneider R, Taccogna F, Hatayama A, Longo S, Capitelli M, Tskhakaya D and Bronold F X 2007 *Contrib. Plasma Phys.* **47** 595
- [94] Phelps A V [http://jila.colorado.edu/avp/collision\\_data/](http://jila.colorado.edu/avp/collision_data/) unpublished
- [95] Phelps A V 1994 *J. Appl. Phys.* **76** 747
- [96] Kollath R 1956 *Secondary Electron Emission of Solids Irradiated by Electrons (Encyclopedia of Physics vol 21)* ed S Fluegge (Berlin: Springer)
- [97] Phelps A V and Petrovic Z L 1999 *Plasma Sources Sci. Technol.* **8** R21
- [98] Daksha M, Berger B, Schuengel E, Korolov I, Derzsi A, Koepke M, Donkó Z and Schulze J 2016 *J. Phys. D: Appl. Phys.* **49** 234001
- [99] Lee Y-K and Chung C-W 2011 *J. Appl. Phys.* **109** 013306
- [100] Gudmundsson J T, Lundin D, Stancu G D, Brenning N and Minea T M 2015 *Phys. Plasmas* **22** 113508
- [101] Matsunami N, Yamamura Y, Itikawa Y, Itoh N, Kazumata Y, Miyagawa S, Morita K, Shimizu R and Tawara H 1984 *Atomic Data Nucl. Data Tables* **31** 1